Lessons Learned From Multiple Fidelity Modeling of Ground Interferometer Testbeds

S.S. Joshi[a] and G.W. Neat[b]

[a] Jet Propulsion Laboratory, California Institute of Technology

[b] Jet Propulsion Laboratory, California Institute of Technology

ABSTRACT

The MicroPrecision Interferometer Testbed (MPI) at JPL is a dynamically and dimensionally representative hardware model of a future spaceborne optical interferometer.[1] Over the past few years, several models of MPI have been created. These include detailed, high-fidelity models of MPI and several lower-fidelity models. These models were meant to answer two basic questions: (1) "Does current modeling methodology allow accurate models of highly complex opto-mechanical systems such as the MPI testbed?" and (2) "Given a valid modeling methodology, how much model fidelity is needed in models to accurately predict performance?". In order to answer these questions, four models of the MPI testbed were created; each with a unique optical and structural model fidelity. This paper reviews results obtained from these models. It compares disturbance transfer function predictions from three of the models with measured disturbance transfer functions from the hardware testbed. (The fourth model, not discussed here, quantifies the effects of model-updating using both modal and in-situ component testing.[2]) Results suggest that it is possible to build a highly accurate high-fidelity model, thus validating the modeling methodology. With lower fidelity models, meaningful model prediction errors exist when simple models are used to represent the complex opto-mechanical system. However, modest increases in model fidelity can lead to significant improvement.

Keywords: Interferometer, MPI, modeling, IMOS

1. INTRODUCTION

Discovery of earth-like planets around other stars requires an instrument with micro-arcsecond astrometric measurement accuracy.[1,3] Spaceborne optical interferometers are likely to be the first instrument class capable of achieving this accuracy level. Although this partial-aperture approach offers a number of important advantages over the traditional full-aperture approach (*e.g.*, the Hubble Space Telescope), the instrument requires stabilization of optical elements down to the nanometer level as well as laser metrology resolution at the picometer level.[4] The charter for the JPL Interferometer Technology Program (ITP) is to mitigate risk for this optical interferometer mission class.[5] A number of ongoing complementary activities address these technology challenges. These activities are: integrated modeling methodology development and validation, metrology and vibration hardware testbed development, and flight qualification of the interferometer components. Though all of these activities are necessary to buy down mission risk, it is integrated modeling that ultimately will be used in the mission and instrument design.

In anticipation of these modeling needs, the Integrated Modeling of Optical Systems (IMOS) and the Controlled Optics Modeling Package (COMP) software packages were developed at JPL.[6,7] These packages allow an integrated modeling methodology that combines structural modeling, optical modeling, and control system design within a common software environment. Several important issues have been addressed using this software. The first important issue was whether the integrated modeling methodology developed had the necessary capability to meet the demanding analysis needs of interferometry modeling. The Micro-Precision Interferometer (MPI) testbed provided an excellent test article to validate modeling methodology. MPI is a dynamically and dimensionally representative hardware model of a future spaceborne optical interferometer (see Figure 1).[1] In order validate the integrated modeling methodology, a highly detailed, high-order model of MPI was constructed. In addition, this model was updated using test data from both modal and in-situ component testing.[2]

(Send correspondence to S. Joshi, MS198-326, Jet Propulsion Laboratory, 4800 Oak Grove Drive, Pasadena, CA 91109)
S.S. Joshi: E-mail: sanjay.s.joshi@jpl.nasa.gov
G.W. Neat: E-mail: neat@huey.jpl.nasa.gov

Once the highly detailed model of the interferometer was completed, it was clear that producing such a model was a very time consuming and costly task. Furthermore, the larger the model, the more unwieldy it became to exercise. Conversely, lower fidelity models would take considerably less time to build and execute. Therefore, an effort was initiated to study how lower fidelity models would predict performance as compared to the high fidelity model. It was clear that the results from lower fidelity models would be in question if the simple models did not accurately represent the real problem. In developing lower fidelity models, careful consideration must be taken to maintain model fidelity where it significantly impacts performance prediction and simplify where it does not.

Thus, two more lower-fidelity models of the MPI testbed were created; each with a unique optical and structural model fidelity. Disturbance transfer functions, measured from the attachment point of the primary disturbance source (spacecraft reaction wheel assemblies) to output optical sensors, were the primary measurements used for instrument performance assessment. These transfer functions accurately depict (in a linear sense) the effectiveness of vibration attenuation strategies at achieving nanometer stabilization of optical elements on a large, lightly-damped, flexible structure excited by mechanical vibrations. This paper, then, describes the three models (one high-fidelity and two lower-fidelity) and compares the predicted disturbance transfer functions from each with the actual measured disturbance transfer function from the testbed.

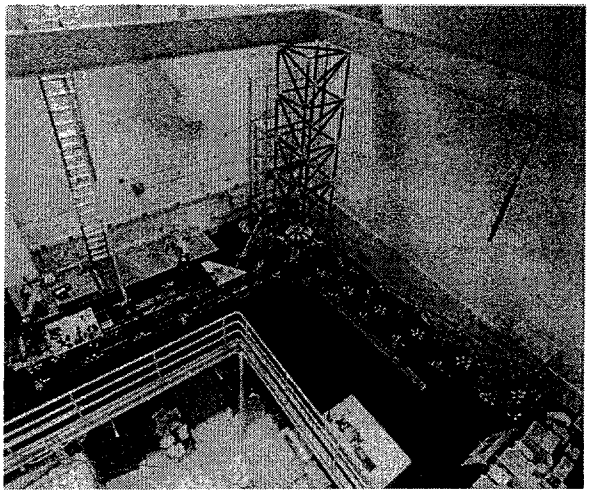

Figure 1. Bird's-eye view of the MPI Testbed.

2. MPI TESTBED DESCRIPTION

Figure 1 shows a bird's-eye view of the testbed which contains all the systems necessary to perform a space-based, optical interferometer measurement. From the entrance apertures all the way through to the optical detectors, the stellar beam bounces off twenty-seven optical surfaces which are distributed across a 7m truss structure. Three appendages make up the base structure which is composed of drawn-wall aluminum struts. The optical mounting design strategy was to group the optical elements that were close in proximity and mount these groups on independent, locally stiff plates. These plates attached kinematically to the structure. Each individual optic is mounted on a stiff mirror mount which clamps to the respective mounting plate.

3. MPI HIGH-FIDELITY INTEGRATED MODEL

The MPI *high-fidelity* integrated model consists of a structural finite element model and a linear optical model that are integrated together. The structural model is generated with IMOS, whereas both IMOS and COMP [7] are used to create the optical model. The integration and analysis are performed in MATLAB [8] with the aid of IMOS functions.

3.1. High-fidelity Structural Model

The structural model is specified in IMOS as a finite element geometry, shown in Figure 2. This geometry consists of plate, beam, truss, and rigid body elements, modeling the base truss structure and the components. The base

truss structure is made up of three booms: the horizontal optics boom, the vertical tower, and the canted metrology boom. The components consist of inboard and outboard optics plates, a disturbance mount plate, two siderostat mounts, an optics cart containing an active delay line, the optics cart support structure, a hexapod isolation system, a passive delay line, and an external metrology beam launcher plate. The finite element model uses 2,577 degrees of freedom (dof) of which 1,832 dofs are independent with respect to the multi-point constraints (MPCs) of the rigid body elements (RBEs).[6]

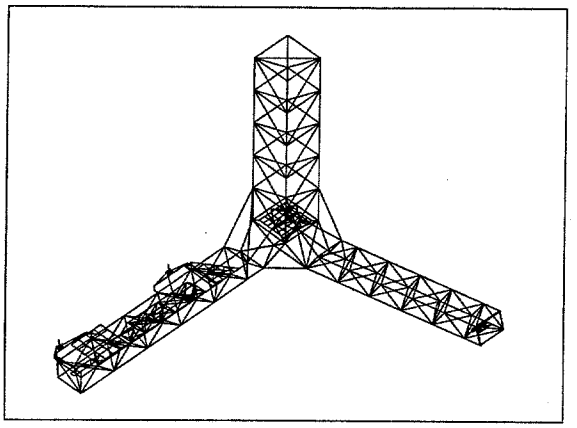

Figure 2. The High-Fidelity model.

The plate and beam properties as well as the finite element geometry itself have been refined by incorporating MPI modal test data into the model. The structural model updating has been done in two phases, following the phased delivery of the MPI testbed. The first phase involved estimating the parameters of the beams comprising the base truss structure from modal testing performed on the bare truss.[9,10] The second phase involved geometry modification and parameter estimation of the optics cart support structure, using *in situ* component modal test data.[11,12] A separate study, not described here, has quantified the effects of this model updating on performance prediction accuracy.[2]

From the finite element geometry and its associated properties the system mass and stiffness matrices are built. The result is a second-order, state-space description of the form:

$$M\ddot{d} + Kd = B_f f \tag{1}$$

where M and K are the system mass and stiffness matrices, d is the nodal state, f is a vector of force input, and B_f is the force influence matrix.

After the system mass and stiffness matrices are built, multi-point constraints are generated using RBE elements. These constraints take the form of[6]:

$$d = \begin{bmatrix} d_n \\ d_m \end{bmatrix} = \begin{bmatrix} I_n \\ G_m \end{bmatrix} d_n = G d_n \tag{2}$$

where d_n are the independent degrees of freedom and d_m are the dependent degrees of freedom. These constraints are then applied to Equation 1, reducing the state of the system to the independent degrees of freedom:

$$\begin{aligned} G^T M G \ddot{d}_n + G^T K G d_n &= G^T B_f f \\ M_{nn}\ddot{d} + K_{nn} d &= B_{nf} f \end{aligned} \tag{3}$$

The eigensolution of Equation 3 is found, yielding flexible-body modes and modeshapes. The resultant diagonalized system is:

$$\begin{aligned} \ddot{\eta} + 2Z\Omega\dot{\eta} + \Omega^2\eta &= \Phi_n^T B_{nf} f \\ d &= G\Phi_n \eta \end{aligned} \tag{4}$$

where η is the modal state vector, Z is a diagonal modal damping matrix, Ω is the diagonal modal frequency matrix, and Φ_n is the eigenvector matrix. Z is formed by assuming a modal damping of 0.3% for flexible body modes above 32 Hz and damping ranging from 0.15% to 0.45% for modes below 32 Hz. These damping values correspond to estimates obtained from the second phase of modal tests.

3.2. High-fidelity Optical Model

The optical model begins with a specification of the optical prescription. This prescription includes the shapes, positions, and orientations of the optical elements. A ray trace of the optical prescription is shown in Figure 3. This optical prescription is generated in IMOS based on the prescription of the actual optical elements of MPI. The model generation uses the structural finite element geometry in order to simplify the prescription definition and to ease the succeeding structural-optical model integration. This allows the location of the actual optical elements to be measured with respect to reference points on the structure as opposed to with each other. Furthermore, structural nodes that correspond to optical element attachment points are easily identified or defined.

Once the optical prescriptions are specified, they are exported to COMP, where linear optical models are created. These linear models are calculated by performing an analytic differential ray trace.[7] The result is a model of the form:

$$y = C_{opt} d \tag{5}$$

where d is a vector of optical element position and orientation perturbations, y is a vector of optical output, and C_{opt} is the optical sensitivity matrix. The optical output can be pathlength, wavefront tilt, or spot motion.

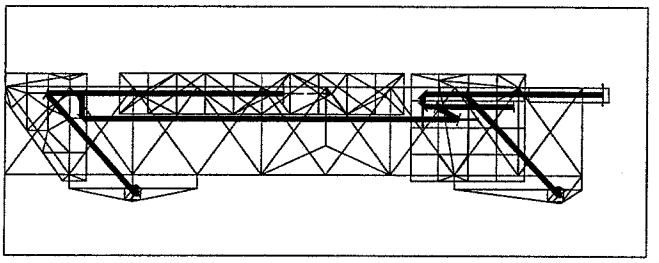

Figure 3. The High-Fidelity optical model.

3.3. Structural-Optical Model Integration

Once the structural modal model and the linear optical model have been created, they are integrated to form a structural-optical model. This integrated model is specified in first-order, state-space from, lending itself most easily to analysis with existing MATLAB functions. In particular, the state-space integrated model can be used for frequency-domain analysis, time-domain simulation, and closed-loop synthesis.

First, the structural model is truncated to remove modes above the bandwidth of expected disturbances (*i.e.*, above 900 Hz).[13,14] The truncated modal model is then converted into first-order, state-space form by using the substitution[6]:

$$x = \begin{bmatrix} \eta_k \\ \dot{\eta}_k \end{bmatrix} \tag{6}$$

Resulting in:

$$\begin{aligned} \dot{x} &= Ax + Bu \\ d &= C_d x + Du \end{aligned} \tag{7}$$

with:

$$\begin{aligned} A &= \begin{bmatrix} 0 & I \\ -2Z_k\Omega_k & -\Omega_k^2 \end{bmatrix} \quad B = \begin{bmatrix} 0 \\ \Phi_{nk}^T G^T B_f \end{bmatrix} \\ C_d &= \begin{bmatrix} G\Phi_{nk} & 0 \\ 0 & G\Phi_{nk} \end{bmatrix} \qquad D = 0 \end{aligned} \tag{8}$$

where the subscript k refers to the set of kept modeshapes.

Finally, the linear optical model is incorporated into the first-order model. The optical output is obtained by premultiplying d by the optical sensitivity matrix, C_{opt}. In this case the matrix C of the measurement equation of Equation 7 becomes:

$$C = C_{opt} C_d \tag{9}$$

Note that the matrix D of Equation 7 is still zero but now has different dimension.

4. LOWER FIDELITY MODEL DESCRIPTIONS

4.1. Low-Fidelity Structural Model

Figure 4 shows the structural model for both the *Low-Fidelity* and *Mid-Fidelity* models.

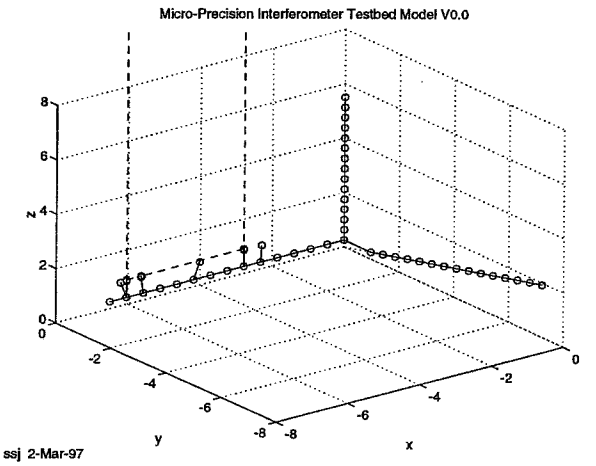

Figure 4. The Low-Fidelity and Mid-Fidelity structural model. Dotted lines show optical path for *Low-Fidelity* model.

The *Low-Fidelity* model consists of three beams to model the MPI truss. Individual strut properties that make up the actual MPI testbed were used to calculate effective beam properties. Optical plates and individual components are modeled only as point masses. These include two siderostat masses, two delay line masses, two optical plate masses (which include all optics mounted on them), a metrology beam launcher mass and an isolation system mass. The mounts for the elements are modeled as rigid connections to the beams.

The *Mid-Fidelity* model consists of three beams to model the MPI truss. Individual strut properties that make up the actual MPI testbed were used to calculate effective beam properties. Optical plates and individual components are modeled only as point masses, just as in the Low-Fidelity model. The mounts for the elements (except the metrology beam launcher mass and isolation system mass) are now modeled as uncoupled, six degree-of-freedom springs from the center of mass of the elements to the beams. The stiffnesses for these springs were derived from high fidelity models of the components.

For all models, a modal damping of 0.3% is assumed for the global flexible-body modes, and a damping, where appropriate, of $\approx$ 3% is assumed for the dynamics associated with the delay line structure. These damping values are consistent with estimates obtained from modal tests.

4.2. Optical Model

The *Low-Fidelity* optical model (Figure 4) contains five optical surfaces: two siderostats, two beam combiner mirrors, and a fringe detector. The *Mid-Fidelity* optical model (not shown) contains ten optical surfaces: two siderostats, one steering mirror, four delay line mirrors, two beam combiner mirrors, and a fringe detector.

Comparison of MPI Models			
-	No. DOF	No. Modes	No. Opt. Elems.
Low	336	92	5
Mid	372	112	10
High	2577	579	27

Table 1. Comparison of number degrees of freedom, number of modes under 900 Hz, and number of optical elements.

4.3. Model Comparison

Table 1 gives an overview of important features of each of the three models after structural-optical model integration (see section 3.3) and modal truncation.

5. COMPARISON METHOD

5.1. Approach

Interferometer performance is primarily degraded by variation in optical pathlength difference (OPD), i.e., the difference in the distances that the light travels from the stellar source, through each arm of the interferometer to the interference optical detector. This difference must be stabilized to the 10 nm (RMS) level in the on-orbit mechanical disturbance environment. It is expected that the dominant disturbance will be the high frequency harmonics from the reaction wheel assemblies that result from bearing imperfections, wheel imbalances, etc.

In contrast to estimating modal characteristics as in,[11,12] disturbance input (at the reaction wheel location) to stellar OPD output transfer functions were measured since they completely characterize (in a linear sense) the propagation of disturbances to OPD. Therefore, in this study, these disturbance transfer functions were predicted by the three different models and compared with the measured disturbance transfer function from the testbed.

5.2. MPI Measurement

Figure 5 shows the disturbance input location relative to the OPD output location for the MPI testbed. This disturbance transfer function was measured for three force disturbance directions: (x, y, z). An HP data analyzer was used to collect the data. A 10 N shaker, mounted at the base of the tower, applied the force input in each of the three directions. The force input was measured with a load cell mounted between the shaker and the structure. The analyzer calculated the transfer function from force input to OPD output.

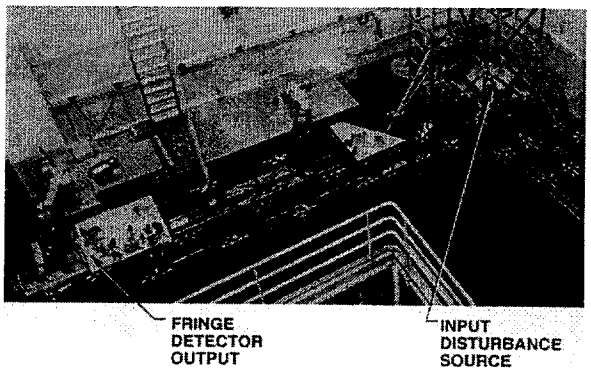

Figure 5. Locations of disturbance input and OPD output on the MPI testbed.

5.3. Comparison Metric

In general on space-based interferometers, mechanical disturbances will be either broadband or narrowband with the energy varying over broad frequency ranges as a function of time.[13,14] In either case, the power spectral density of the disturbance is broadband. Therefore, the integrated model should be accurate in a broadband sense. More specifically, we desire σ_{opd} to be accurate, where[15]:

$$\sigma_{opd}^2 = \frac{1}{\pi}\int_0^\infty |G(\jmath\omega)|^2 \Phi_d(\omega) d\omega \tag{10}$$

for a broadband disturbance power spectral density, $\Phi_d(\omega)$, and a disturbance to OPD transfer function, $G(\jmath\omega)$.

Since Equation 10 yields the quantity that we wish to accurately predict, we can use this same equation as a metric to characterize the measured and predicted transfer functions. As opposed to picking a particular expected disturbance power spectral density, bandlimited white noise (over $[\omega_{min}, \omega_{max}]$) is used:

$$\sigma_g^2 = \frac{A_d}{\pi}\int_{\omega_{min}}^{\omega_{max}} |G(\jmath\omega)|^2 d\omega \tag{11}$$

where A_d is the amplitude of the bandlimited white noise disturbance power spectral density with ω_{min} and ω_{max} defining the frequency range of interest. σ_g is used instead of σ_{opd} in order to stress that the result is a metric of the transfer function itself.

Using this metric, the accuracy of the model can be quantified by comparing σ_g for the *Low-Fidelity*, *Mid-Fidelity*, *High-Fidelity* and measured transfer functions. As such, the particular value of the disturbance amplitude is immaterial. The amplitude is chosen so that the variance of the disturbance is one. This choice is arbitrary, and the value of σ_g has no significance by itself. It is the *comparison* of the metrics for corresponding measured and predicted transfer functions that is meaningful.

5.4. High Fidelity Results

Generally, it is desired that OPD variation predictions be accurate to within a factor of 2. Since the metric σ_g is closely related to OPD variations for broadband noise, the factor of 2 is applied as a requirement to the ratio of σ_g for the measured and predicted transfer functions.

The modulus of the measured transfer functions, along with the corresponding predicted transfer functions, are shown in Figures 6-8. The predicted transfer functions were calculated by applying standard MATLAB functions to the integrated model with disturbance force input and OPD output. The value of the broadband metric, also calculated with MATLAB functions, is given in the legend for each transfer function.

The results of these comparisons are shown in Table 2. The bandwidth of interest is [4, 900] Hz. Below 4 Hz the force capability of the shaker is limited and the testbed suspension modes pollute the measurement. Above 900 Hz the mechanical disturbances are expected to have no energy. This bandwidth is further broken roughly into decades and comparisons are shown for these "decades." Units are not given in the table so as to discourage the reader from attaching significance to the separate values.

The comparisons for the three force disturbance transfer functions show that the broadband metrics ([4, 900] Hz) for the predicted transfer functions are accurate with respect to the measured transfer functions to well within the desired factor of two. Furthermore, the comparisons for each "decade" show accuracies of better than a factor of three. This indicates that OPD variation estimates for colored broadband input should also be accurate.

5.5. Lower Fidelity Results

The modulus of the measured transfer function, along with the corresponding predicted transfer functions, are shown for the z-force input disturbance to OPD output case (Figures 9-10). Again, the predicted transfer functions were calculated by applying standard MATLAB functions to the integrated models with disturbance force input and OPD output. The results of comparisons for z force inputs are shown in Table 3. The trends are similar for the x and y directions.

The *Low-fidelity* model shows good performance in the low frequency range (4 - 10 Hz) and a degradation in performance at higher frequencies. This is to be expected since the simple beam model will capture global modes well, but not local modes caused by individual mounts or individual truss elements. The *Mid-fidelity* model added simple mount models. This increased performance of the model, especially in the mid frequency range (10 - 110 Hz).

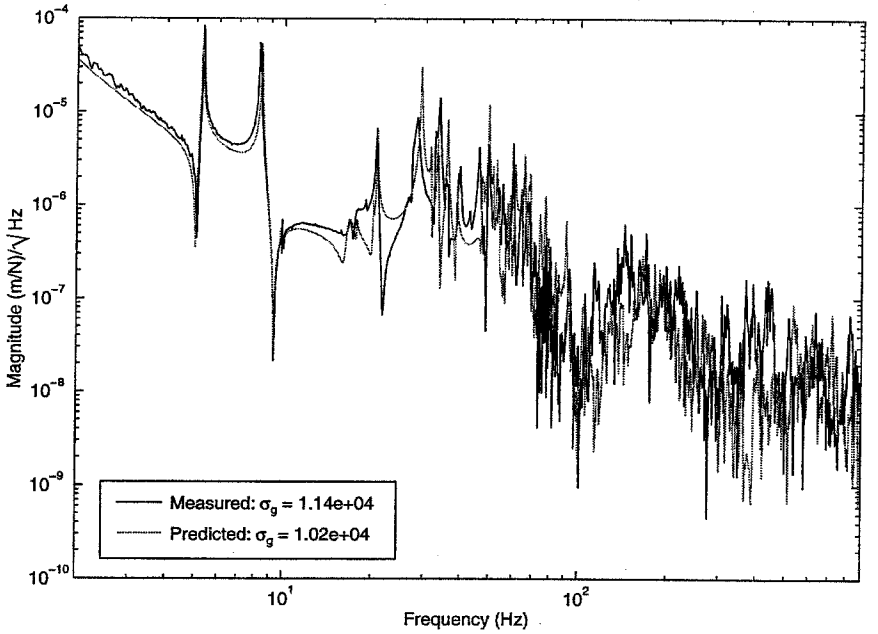

Figure 6. Predicted and measured MPI disturbance to OPD transfer function: x-axis force input.

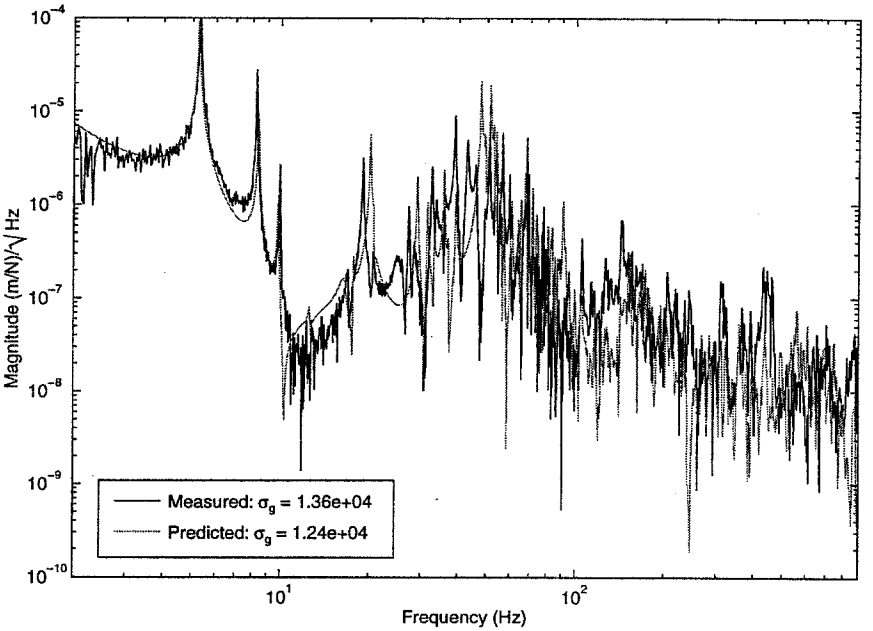

Figure 7. Predicted and measured MPI disturbance to OPD transfer function: y-axis force input.

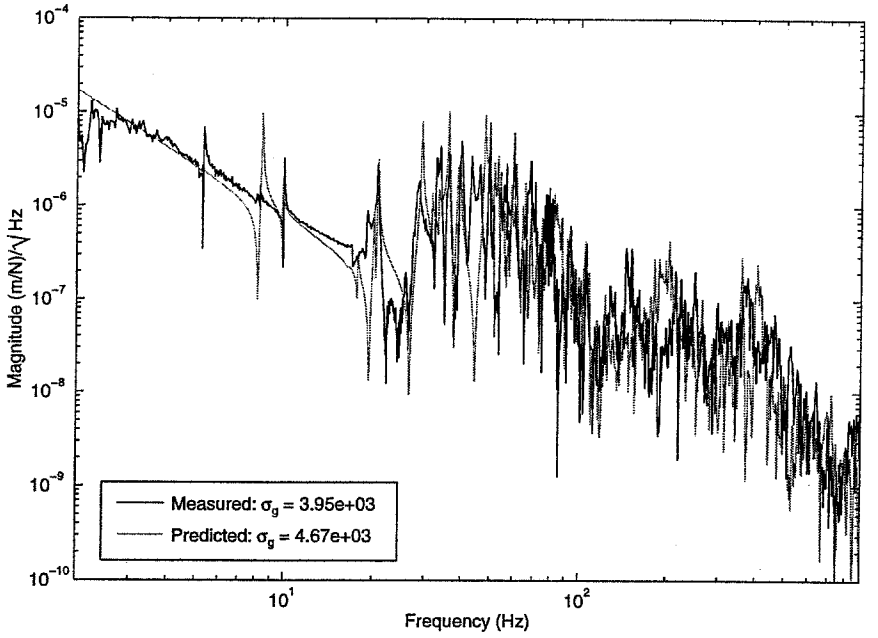

Figure 8. Predicted and measured MPI disturbance to OPD transfer function: z-axis force input.

Disturbance Input		σ_g			
		4 - 10 Hz	10 - 100 Hz	100 - 900 Hz	*4 - 900 Hz*
x-axis Force	meas	9,971	5,415	698	*11,368*
	pred	7,543	6,928	373	*10,249*
	factor	0.76	1.28	0.53	*0.90*
y-axis Force	meas	13,132	3,603	695	*13,635*
	pred	10,165	7,182	310	*12,450*
	factor	0.77	1.99	0.45	*0.91*
z-axis Force	meas	1,851	3,457	498	*3,953*
	pred	1,777	4,287	555	*4,674*
	factor	0.96	1.24	1.11	*1.18*

Table 2. Broadband transfer function metric comparison between the predicted and measured transfer functions of the MPI Testbed.

6. CONCLUSION/FUTURE WORK

This paper investigates the model prediction capabilities of models of varying structural and optical complexity. A metric is used that characterizes the disturbance transfer functions over a broad frequency range. This metric is simply the expected OPD variation assuming a bandlimited white noise disturbance input. Comparison of the three models shows that a *High-fidelity* model predicts test results well, thus validating the open-loop modeling methodology. The *Low-fidelity* model shows good performance in the low frequency range (4 - 10 Hz) and a degradation in performance at higher frequencies. This is to be expected since the simple beam model will capture global modes well, but not local modes caused by individual mounts or individual truss elements. The *Mid-fidelity* model added simple mount models. This increased performance of the model, especially in the mid frequency range (10 - 110 Hz). It should be noted that most mount modes were located in this range. Overall, the modest increase in fidelity from the *Low-fidelity* to *Mid-fidelity* model helped performance significantly .

This paper only addresses the hardmounted-disturbance, open-loop-control configuration. Validation of the

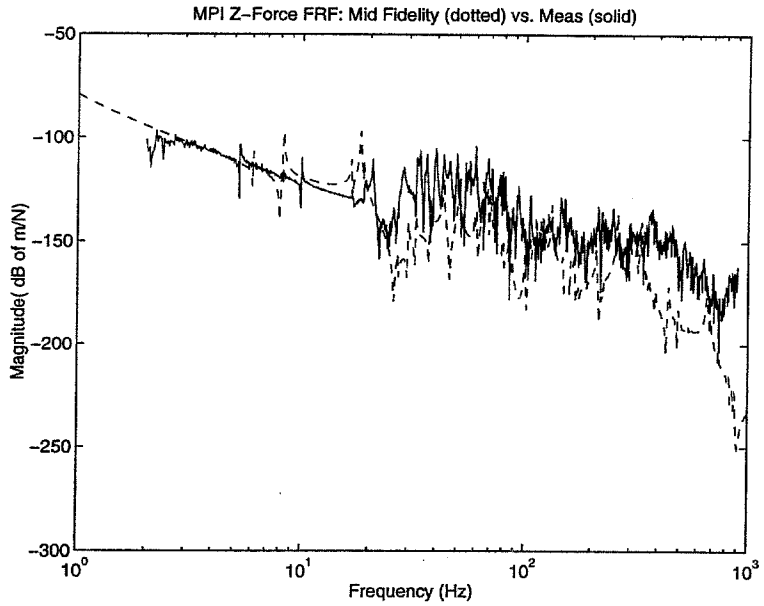

Figure 9. Comparison of measured data from test article to Mid-fidelity model MPI disturbance to OPD transfer function: z-axis force input.

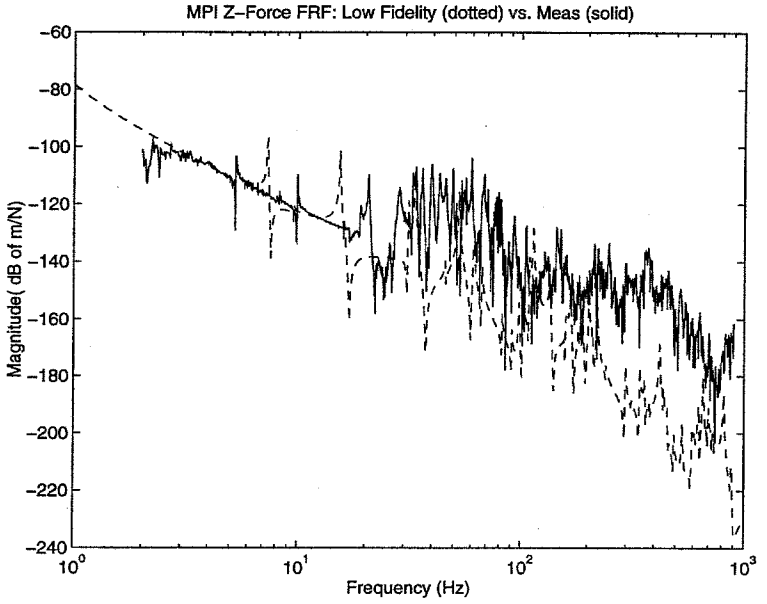

Figure 10. Comparison of measured data from test article to Low-fidelity model MPI disturbance to OPD transfer function: z-axis force input.

methodology for various closed-loop configurations has been described in other sources.[16] In the future, we intend to add additional models in our suite of models to explore when adding more fidelity leads to a diminishing rate of returns.

Acknowledgements

This work was performed at the Jet Propulsion Laboratory, California Institute of Technology, under contract with the National Aeronautics and Space Administration. This work was made possible by the efforts of several JPL

Disturbance Input		σ_g			
		4 - 10 Hz	10 - 110 Hz	110 - 900 Hz	*4 - 900 Hz*
z-axis Force	Low	1.198	0.410	0.345	*0.667*
	Mid	1.212	0.740	0.368	*0.863*
	High	0.928	1.492	0.790	*1.380*
	Test	1.000	1.000	1.000	*1.000*

Table 3. Transfer function metric comparison between the low-fidelity model, mid-fidelity model, high-fidelity model and measured (test) transfer functions of the MPI Testbed. All numbers normalized with respect to test values.

researchers including Alex Abramovici, Robert J. Calvet, Renaud Goullioud, Robert P. Korechoff, M. Levine, J. Melody, Gregory W. Neat, and Sanjay S. Joshi.

REFERENCES

1. G. W. Neat, A. Abramovici, J. W. Melody, R. J. Calvet, N. M. Nerheim, and J. F. O'Brien, "Control technology readiness for spaceborne optical interferometer missions," in *Proc. Space Microdynamics and Accurate Control Symposium*, (Toulouse, France), May 1997.
2. S. S. Joshi, J. W. Melody, G. W. Neat, and A. Kissil, "Benefits of model updating: A case study using the micro-precision interferometer testbed," in *Proc. 16th ASME Biennial Conference on Mechanical Vibration and Noise*, (Sacramento, CA), Sept. 1997.
3. B. F. Burke, ed., *TOPS: Towards Other Planetary Systems*, National Aeronautics and Space Administration, Solar System Exploration Division, Washington, D.C., 1992.
4. M. Shao and D. M. Wolff, "Orbiting stellar interferometer," in *Spaceborne Interferometry II*, R. D. Reasenberg, ed., vol. 2447 of *Proc. SPIE*, pp. 228–239, (Orlando, FL), Apr. 1995.
5. R. A. Laskin, "Technology for space optical interferometry," in *Proc. 33rd Aerospace Sciences Meeting and Exhibit*, vol. 95–0825, AIAA, (Reno, NV), Jan. 1995.
6. M. H. Milman, H. C. Briggs, W. Ledeboer, J. W. Melody, R. L. Norton, and L. Needels, *Integrated Modeling of Optical Systems User's Manual, Release 2.0*, Nov. 1995. JPL D–13040 (JPL Internal Document).
7. D. Redding, *Controlled Optics Modelling Package User Manual, Release 1.0*, June 1992. JPL D–9816 (JPL Internal Document).
8. The Math Works Inc., *Matlab User's Guide*, Aug. 1992.
9. T. G. Carne, R. L. Mayes, and M. B. Levine-West, "A modal test of a space-truss for structural parameter identification," in *Proc. 11th IMAC*, (Kissimmee, FL), Feb. 1993.
10. J. R. Red-Horse, E. L. Marek, and M. B. Levine-West, "System identification of the jpl micro-precision interferometer truss: Test-analysis reconciliation," in *Proc. 34th SDM*, (La Jolla, CA), Apr. 1993.
11. M. B. Levine-West and J. W. Melody, "Model updating of evolutionary structures," in *Proc. 15th ASME Biennial Conference on Mechanical Vibration and Noise*, (Boston, MA), Sept. 1995.
12. J. W. Melody and M. B. Levine-West, "High fidelity modeling of evolutionary structures in IMOS," in *Proc. First World Conference on Structural Control*, pp. WP1–98 to WP1–107, (Los Angeles, CA), Aug. 1994.
13. J. W. Melody and H. C. Briggs, "Analysis of structural and optical interactions of the precision optical interferometer in space (POINTS)," in *Spaceborne Interferometry*, R. D. Reasenberg, ed., vol. 1947 of *Proc. SPIE*, pp. 44–57, (Orlando, FL), Apr. 1993.
14. S. Shaklan, J. Yu, and H. C. Briggs, "Integrated structural and optical modeling of the orbiting stellar interferometer," in *Space Astronomical Telescope and Instrument II*, Proc. SPIE, (Orlando, FL), Apr. 1993.
15. A. Papoulis, *Probability, Random Variables, and Stochastic Processes*, McGraw-Hill, New York, 3rd ed., 1991.
16. J. W. Melody and G. W. Neat, "Integrated modeling methodology validation using the micro-precision interferometer testbed: Assessment of closed-loop performance prediction capability," in *Proc. American Control Conference*, (Albuquerque, NM), June 1997.